3D printed Ni/Al_2O_3 based catalysts for CO_2 methanation - a comparative and operando XRD-CT study

Vesna Middelkoop [a], Antonis Vamvakeros[b,c], Dieter de Wit [a,d], Simon D. M. Jacques[b], Simge Danaci [a,e], Clement Jacquot[a,f], Yoran de Vos [a,g], Dorota Matras [b], Stephen W. T. Price[b], Andrew M. Beale[b,f,h]

a) Sustainable Materials Management, Flemish Institute for Technological Research, VITO NV, Boeretang 200, Mol, Belgium.
b) Finden Ltd, Merchant House, 5 East St Helen Street, Abingdon, Oxfordshire OX14 5EG, UK
c) ESRF, 6 Rue Jules Horowitz, 38000 Grenoble, France.
d) University Colleges Leuven-Limburg, Agoralaan B, 3590 Diepenbeek, Belgium
e) Grenoble Alpes University, CEA, LITEN, 17 rue des Martyrs, F-38054 Grenoble, France
f) Department of Chemistry, University College London, 20 Gordon Street, London WC1H 0AJ, UK
g) Department of Chemistry, Center for Ordered Materials, Organometallics and Catalysis (COMOC), Faculty of Sciences, Ghent University, Krijgslaan 281, 9000 Ghent, Belgium
h) Research Complex at Harwell, Rutherford Appleton Laboratory, Didcot, OX110FA, UK

Abstract

Ni-alumina-based catalysts were directly 3D printed into highly adaptable monolithic/multi-channel systems and evaluated for CO_2 methanation. By employing emerging 3D printing technologies for catalytic reactor design such as 3D fibre deposition (also referred to as direct write or microextrusion), we developed optimised techniques for tailoring both the support's macro- and microstructure, as well as its active particle precursor distribution. A comparison was made between 3D printed commercial catalysts, Ni-alumina based catalysts and their conventional counterpart, packed beds of beads and pellet. Excellent CO_2 conversions and selectivity to methane were achieved for the 3D printed commercial catalyst (95,75 and 95,63 % respectively) with stability of over 100 h. The structure-activity relationship of both the commercial and in-house 3D printed catalysts was explored under typical conditions for CO_2 hydrogenation to CH_4, using *operando* 'chemical imaging', namely X-Ray Diffraction Computed Tomography (XRD-CT). The 3D printed commercial catalyst showed a more homogenous distribution of the active Ni species compared to the in-house prepared catalyst. For the first time, the results from these comparative characterisation studies gave detailed insight into the fidelity of the direct printing method, revealing the spatial variation in physico-chemical properties (such as phase and size) under operating conditions.

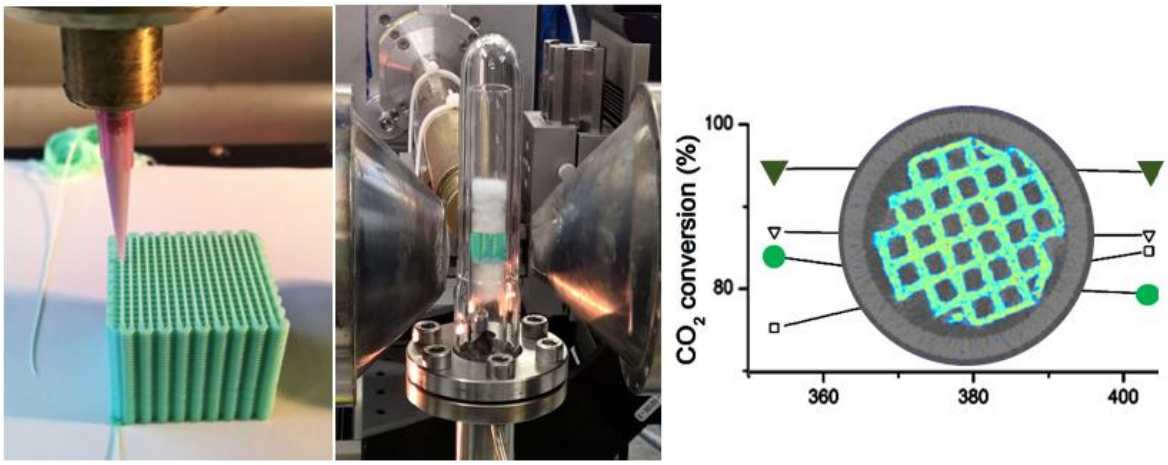

1. Introduction

The utilisation of CO_2 as a feedstock in the chemical industry for the synthesis of various chemical products offers great potential for meeting CO_2 emissions reduction targets, while increasing independence from fossil fuels.[1] Since the energy is required to convert CO_2 to value added products it is only possible to deliver low-carbon energy solutions when CO_2 conversion technologies are combined with surplus renewable electricity transformed into hydrogen (via electrolysis of water).[2] The direct catalytic hydrogenation of CO_2 such as methanation (also referred to as the Sabatier reaction) is pertinent to the present drive towards maximising the potential of renewable power-to-gas applications for converting hydrogen into synthetic methane by reaction with CO_2.[3,4,5] Power-to-gas CO_2 methanation processes are already at an advanced stage of development towards commercial application, capable of the utilisation of 1 tonne of CO_2 per tonne of synthetic natural gas (SNG) product, employing proprietary catalyst formulations with conversions of up to 100 % at relatively low temperatures and high pressures.[6, 7,8]

Alongside the development of microchannel reactors for CO_2 methanation[9,10], two classes of well-known structured reactors employing high surface-to-volume ratio supports have been reported in the literature on novel reactor designs for the methanation reaction, namely monolithic honeycomb supports and foams. In comparison to their conventional counterparts (packed bed reactors), monolithic honeycombs offer a controllable low pressure drop and heat transfer (in particular the metallic monoliths) but lack radial mass transport[11,12,13,14,15], while foam structures provide good radial heat and mass transfer but an higher (adjustable) pressure drop due to their random porous structure.[16, 17]

The burgeoning demand for 3D printing technology for functional materials design is due to its suitability to produce structured arrays by well-controlled deposition of both sacrificial and active material with a wealth of potential applications in chemistry, biology and physics. Largely due to the pioneering work of Lewis and co-workers, direct ink-writing has shown itself to be an attractive and flexible method for patterning and processing functional three-dimensional lattices with architectures and compositions made of a broad range of ink formulations, including concentrated colloidal, nanoparticle and fugitive organic-based inks.[18,19,20,21]

Despite having potential for cross disciplinary synergies, the success of the direct write technique has so far mainly been demonstrated for electronics[22] and biomedical applications[23] with sizes ranging from hundreds of microns to submicrons. The 3D printing (‘direct write’) of catalytically active materials in a variety of compositions has only recently gained wider interest in an attempt

to develop more advanced and efficient alternatives to packed bed reactors and coated honeycomb monoliths.[24,25,26,27,28,29,30,31]

To date, a number of comprehensive thermodynamic and kinetic analyses have been carried out on the proposed CO_2 methanation mechanisms.[32,33,34,35,36,37] The operating parameters used in this work consist of a combination of experimental values previously reported by the authors and others. In particular the work of Gao et al. (2012, 2015) is noteworthy for providing an extensive analysis on the effects of temperature, H_2:CO_2 ratio and pressure on CO_2 methanation.For H_2:CO_2 ratios equal to or more than 4, the CH_4 conversion and yield is thermodynamically favoured at low temperatures (250-350 °C) and high pressure. [38,39]

Although there has been extensive research to date into other heterogeneous formulations (various supports and metal-oxide promotors)[40,41,42,43,44], Ni supported alumina remains among the most widely studied catalysts due to its proven track record within successful systems; it is the most commonly supplied catalyst by major catalyst manufacturers.[45,46,47,48] There has been substantial work conducted into Ni-alumina catalysts for CO_2 methanation with nickel loadings of up to 88%, typically ranging from 10 to 25 wt%.[49,50] A study by Chang et al. (2003) showed that the maximum CH_4 yield and selectivity was obtained at 500 °C for an optimum Ni loading on RHA-Al2O3 of 15- 20 wt.%.[51] Using a Ni/Al_2O_3 catalyst with a loading of 20 wt%, Rahmani et al. (2014) reported the highest values for conversion (83.6%) and CH_4 selectivity (100%) at 350 °C; a further increase in Ni content (25 wt%) showed reduced conversion to CH_4.[52] The most recent and detailed study of Zhang et al. (2019) into the effect of different Ni loadings on alumina showed that the 25 wt% loaded catalysts were the most active, achieving about 60% yield at 400 °C for a H_2:CO_2 ratio of 60:15 mL/min and at 1 atm pressure.[53]

Previous studies of the authors on Ni-alumina coated onto 3D printed metals supports provided further impetus to the development of the directly printed Ni-alumina based monolithic structures for methanation that are presented herein.[54,55]

In this work direct write has been employed for the 3D co-printing of Ni-alumina catalysts to mimick Ni-alumina coated monoliths/honeycombs. By directly patterning the honeycomb-like (multichannel) monolithic catalysts with active materials and supports, a significantly higher degree of control has been achieved over the materials distribution, geometry, morphology and function.

Synchrotron in situ XRD-CT physico-chemical imaging[56,57,58,59,60] has been employed to reveal the fidelity of the direct printing method, as well as the resulting chemical and physical properties of the 3D printed catalyst structures at both the macro- and nanoscale and during the methanation reaction (under operating conditions). SEM and EDX were used to confirm the morphology of the

3D printed structures and the distribution of the Ni particles and alumina support within the structures. The catalytic performance of the 3D printed structures in both an in-house prepared and commercial catalyst powder (mainly nickel on alumina support) was compared to conventional packed beds of beads.

2. Experimental

2.1 Catalyst preparation

The catalysts were prepared by a single step impregnation method whereby nickel nitrate salt in a 0.43 M $Ni(NO_3)_2.6H_2O$ (Panreac) solution was deposited onto alumina powder (Sasol's Puralox TM 100/150 UF) and alumina spheres (Sasol's spheres 1.0/160)[61] to obtain a theoretical loading of 12 wt. % nickel (this loading was selected as representative of a wide range of nickel loadings that have been reported in the recent literature).

The mixtures were stirred until a homogeneous slurry was obtained. Freeze-drying of the slurry was selected as a more suitable method than ambient drying. The Ni-alumina catalyst slurry was dried under vacuum in a HETO Powerdry LL3000 freeze dryer whilst being frozen at a low pressure ensuring that water vapour remained below its triple point. Once the equilibrium had been reached, the temperature was increased and the water content removed from the frozen material by sublimation. After the mixture had completely dried, it was ball milled and sieved with a mesh of 45 µm. The spheres were impregnated by leaving the mixture overnight at room temperature on an orbital shaker platform at ambient temperatures to ensure sufficient adsorption of the nitrate solution into the accessible pores of the spheres. Prior to calcination the spheres were dried at ambient temperature. The impregnated catalyst samples were calcined at 500°C for 2 h with a heating rate of 1-2 °C per minute. This specific temperature was used to ensure a transition of the Puralox powder to a γ-Al_2O_3 phase.

3D periodic tetragonal structures were printed using the in-house produced Ni-alumina catalyst as well as a commercially supplied Ni on γ-Al_2O_3 catalyst from Evonik (composed of 80-85 % γ-Al_2O_3, 3-7 % Ni, and 8-15 % NiO). The structures contained bentonite and alumina-based binders at 18 wt. % on a dry basis to increase their mechanical properties. The 3D printing (direct write) of the homogeneous ink (paste) with the desired and reproducible rheological properties (as described elswhere[54,62,63]) involved extruding and stacking the active material through a deposition nozzle and laying down the filaments into log-pile structures with a 0-90 ° pattern and a spacing of the size of the filament (see Figure 1 showing photos of the printing process). 600

and 800 µm nozzles were used at a printing speed of 700 and 450 µl/min respectively. The structures were subsequently left to dry in a humidity chamber for a week maintained at 85 % RH and 25 °C followed by a thermal pre-treatment at 500˚ C to remove the organic binder from the green printed catalyst bodies.

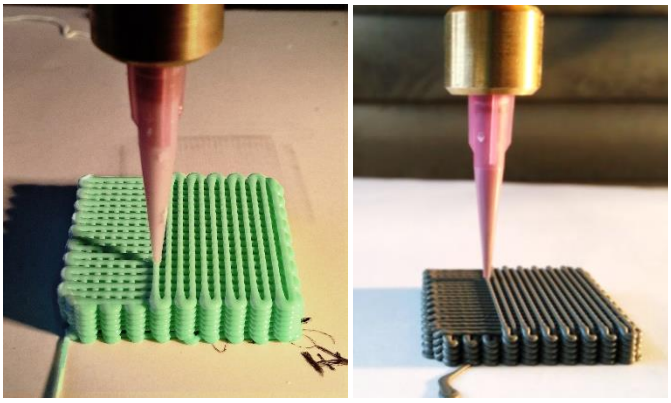

Figure 1. 3D printing of two catalyst materials: in-house synthesised Ni-alumina (left) and commercial catalyst, Octolyst (right).

2.2 Catalyst characterisation

The particle size distribution of the starting and milled powders was determined using a laser diffraction analyser, Microtrac S3500, equipped with a wet dispersion system (SDC) with integrated ultrasound probe for sample dispersion. After the impregnation and calcination of the samples, Ni load loading in the powders and spheres were confirmed by inductively coupled plasma–atomic emission spectrometry (ICP-AES) on an Perkin-Elmer Optima 3000 dv. Nitrogen sorption measurements were performed on a Quantachrome Autosorb-iQ–MP to determine the surface area of the catalysts before and after the reaction using the Brunauer-Emmett-Teller (BET) method. Thermogravimetric analysis (TGA) was performed using a Netzsch STA 449 C Jupiter to yield valuable information on the thermal stability and composition of the 3D printed samples as a function of time. The samples were being gradually heated in an inert gas or dry air flow (of 70 ml min^{-1}) from ambient temperature to 700 °C with a heating rate of 5 °C min^{-1} leading to weight loss (or gain) as a result of a change in the sample's content (e.g. residual water, decomposition of possible organic fractions, polymers, inorganic fillers, carbon black). The TGA equipment was coupled online to an Omnistar GSD 301 O2 (Pfeiffer Vacuum) mass spectrometer.

Conventional lab powder X-ray diffraction (XRD) characterisation was carried out on a Philips/Panalytical X'Pert Pro diffractometer (with Cu Kα source (λ = 1.5418 Å) at 40 kV and 40 mA

at room temperature. Phase identification was carried out using X'Pert High Score Plus software and compared to reference data in the ICDD Powder Diffraction database.

Scanning electron microscopy (SEM) and energy dispersive X-ray (EDX) spectroscopy images were collected using a FEGFEI Nova NanoSEM 450 instrument operating at an accelerating voltage of 25 keV equipped with a Bruker QUANTAX 200 EDX system with an XFlash 5030 SDD detector.

2.3 Catalyst activity

Online gas chromatography (GC) analysis of the concentrations present in the reaction mixture was performed on a Varian 450-GC (Bruker) equipped with two TCDs and one FID detectors (containing Hayesep Q, Hayesep and Molsieve columns arranged in series). GC measurements were performed on the outlet gas mixtures produced from the following sets of catalysis experiments: 1) Ni-Al2O3 3D printed structures with nozzle sizes of 600 and 800 µm 2) Ni- γ-Al_2O_3 and Octolyst pellets (made from crushed 3D printed structures) with sizes ranging from 800 µm to 1000 µm 3) 1.0 mm Ni impregnated alumina spheres. A Hiden HPR-20 gas analysis system (Hiden quadrupole mass spectrometers configured with Electron Impact ionisation) was used for a continuous analysis of outlet gas composition on stream experiments for an extended period of time. *Ex situ* reactions were performed over the pre-reduced catalysts, positioned in the centre of a reactor quartz tube of 13 mm OD and 10 mm ID, which was placed in a Carbolite® tube furnace and connected to the steel tubing with the inlet capillary of the GC or MS.

In all experiments, prior to catalytic testing, the calcined catalysts were reduced *in situ* in the quartz reactor tubes heated with a ramp rate of 1 °C/min to 450 °C, held for 2 h under a flow rate of 100 mL/min (at STP), 80 % H_2 in 20 % He. After the reduction step for each catalyst, the reactor was purged with He and the reaction temperature of the reactor was set to the desired value with the starting temperature of 350 °C. In all reactor tubes, a thermocouple was pushed through the quartz wool inside the reactor to obtain a measurement of the catalyst bed temperature that was as accurate as possible. Three temperatures, 350, 400 and 450 °C, were selected as typical methanation reaction temperatures. In the GC measurements the catalysts were exposed to a flow rate of 40 ml/min of H_2 and 10 ml/min of CO_2 in 150 ml/min of He. The flow rates used in the stability tests were slightly varied and are specified in the caption of the respective figure. Further details on the protocol of the methanation experiments are presented in the Supplementary Information.

2.4 *Operando* studies

Operando XRD-CT measurements at the ESRF ID15A beamline were performed on the in-house Ni-alumina printed catalyst using a monochromatic beam of 78.500 keV focused to a spot size of 30 µm x 30 µm. XRD-CT scans were recorded using interlaced method[64] comprising two angular subsets covering 0 to 180 ° in steps of 1 ° with sample translated over 11 mm in steps of 50 µm (220 steps). Each complete interlaced scan comprised 39,600 diffraction patterns. Each diffraction pattern was acquired over 10 msecs.

A second set of comparative *operando* XRD-CT measurements were carried out on both the 3D printed in-house Ni-alumina catalyst and 3D printed Octolyst catalyst at the same beamline station, ID15A at ESRF. A 90 keV monochromatic X-ray beam was focused to have a spot size of 40 µm x 20 µm (Horizontal x Vertical). The total acquisition time per point was 20 msec and each XRD-CT scan lasted for a total of 20 min. Each XRD-CT scan was made with 171 translation steps (with a translation step size of 40 µm) covering 0 – 180 ° angular range, in 151 steps.

In all runs 2D powder diffraction patterns were collected using a state-of-the-art Pilatus3 X CdTe 2M hybrid photon counting area detector. The detector calibration was performed using a CeO_2 NIST standard. Every 2D diffraction image was converted to a 1D powder diffraction pattern after applying an appropriate filter (i.e. 10 % trimmed mean filter) to remove outliers using pYFAI. The final XRD-CT images (i.e. reconstructed data volume) were reconstructed using the filtered back projection algorithm.

Similar to the lab *ex situ* experiments, the catalyst structures were supported between quartz wool inside a quartz tube. Two types of tubes were used: a tube with an OD of 13 mm, ID of 10 mm and length of 10 mm for the in-house Ni on alumina, and a tube with an OD of 6 mm, ID of 5 mm, and length of 10 mm. The catalyst structures were cut to size to fit snugly into the reactor tube. Figure 2 shows a photograph of the experimental set-up in place at the ID15A beamline. The reactor was mounted onto a motorised stage perpendicular to the beam and on the axis of rotation. The uniform temperature in the catalyst bed was maintained using a set of two heat guns. The gas mixture was delivered through the reactor tube via an inlet valve fitted at the base of the reactor mount. The exit flow was monitored by an Ecosys portable mass spectrometer.

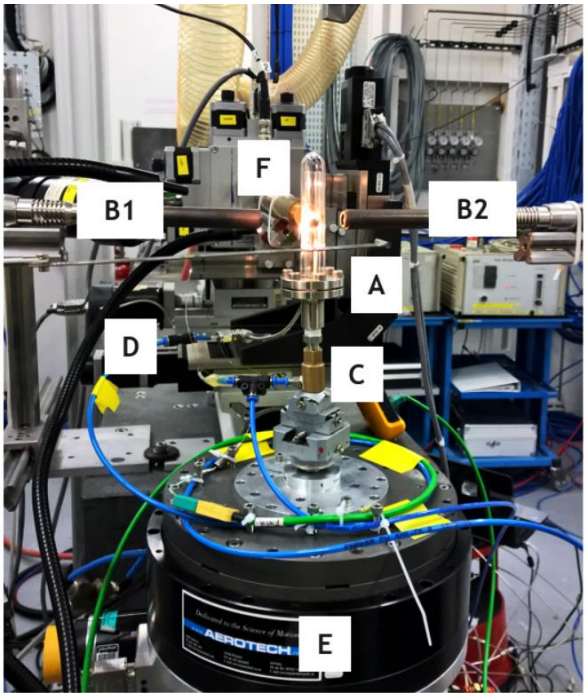

Figure 2. Experimental set-up on beamline ID15 at the ESRF for *in situ/operando* XRD-CT studies: (A) quartz reactor tube loaded with a sample: (B1&2) heat guns, (C) reactor inlet, (D) reactor outlet, (E) rotation stage, (F) incoming beam.

3. Results and discussion

3.1 Catalyst properties

The 3D printed Ni alumina structures showed an increase of approximately 30 % in specific surface area compared to the starting impregnated powder. The 3D printed calcined Octolyst structure shows a slightly higher specific surface area than the 3D printed calcined Ni-alumina powder. It is noteworthy that of all the unused structures, the commercial catalyst had the largest specific surface area.

When comparing the structure before and after the methanation of CO_2, it can be seen that each catalyst (both in the 3D printed form and the spheres) exhibited a decrease in surface area after methanation. The decrease in surface area could be caused by the catalyst shrinkage upon long duration of exposure to high temperatures. The decrease in surface area can be explained by some carbon deposition on the surface of the catalyst. The TGA-MS results on 3D printed reduced and spent Octolyst samples (before and after the reaction respectively) that are shown in Supplementary Figure S1, indicate a low content carbonaceous impurity contributing to a mass loss of 2.9 and 1.9 % corresponding to CO_2 release detected by a mass spectrometer. Similar levels

of residual carbon observed in both the pre- and post reaction samples originate from burning off the printing binder residues.

The specific surface areas derived from nitrogen adsorption isotherms by the BET method are shown in Table 1.

Table 1. Overview of results of BET analysis

Sample	Specific surface area (m^2/g)
Puralox powder as received	135-165
Calcined Ni impregnated alumina powder	109
3D printed (calcined) Ni-alumina structure (600 µm)	150
3D printed (calcined) Ni-alumina structure (800 µm)	157
3D printed Ni-alumina structure after reaction	106
Ni-alumina pellets after reaction	116
Octolyst as-received powder	246
3D printed (calcined) Octolyst structure (800 µm)	177
3D printed Octolyst structure after reaction	152
Alumina 1.0 mm spheres as received	150-170
Ni impregnated 1.0 mm spheres before reaction	156
Ni impregnated 1.0 mm spheres after reaction	129

Both the freeze-dried and Octolyst starting powders were milled to a D90 particle size of roughly 50 µm prior to mixing the printing pastes. However, the cross-sectional SEM images reveal a different, coarser morphology of the 3D printed Ni-alumina structures than that of the 3D printed Octolyst structures. Grains of 5 to up to 50 µm can be observed in the fibre of the 3D printed Ni-alumina catalyst. The SEM images show both the micro and macrostructure of the 3D printed catalysts. SEM/EDX analysis of the spent catalyst did not reveal any obvious changes to the catalyst micro and macrostructure (see the details in the SEM and EDS images shown in the Supplementary Information).

Conventional (*ex situ*) laboratory XRD measurements (presented in Figure 3) show a comparison of the printed calcined, reduced and used printed samples. After the calcination step at 500 °C, peaks corresponding to γ-Al_2O_3 phase could not be completely distinguished as they overlap with the nickel alminate $NiAl_2O_4$ phase present due to the nickel oxide-support interaction. The presence of unreduced $NiAl_2O_4$ can significantly alter catalytic activity; the reducibility of nickel phases is strongly dependent on the calcination temperature. An overall decrease of the $NiAl_2O_4$ presence was observed while NiO was present at 2θ values of 43.5, 50.7 and 74.5° only in the 3D printed calcined Ni-alumina sample. This was followed by the reduction of NiO into Ni which can

clearly be observed in the 3D printed reduced Ni-alumina sample. Ni peaks appear and remain at 2θ of 52.3; 61.1; 92.1 and 115.2° in the 3D printed Ni-alumina structures as well as Ni alumina pellets after reaction. Additionally, small increases of γ-Al2O3 are observed at 54 and 104 2θ°. Further details are provided Figure S2 in the Supplementary Information.

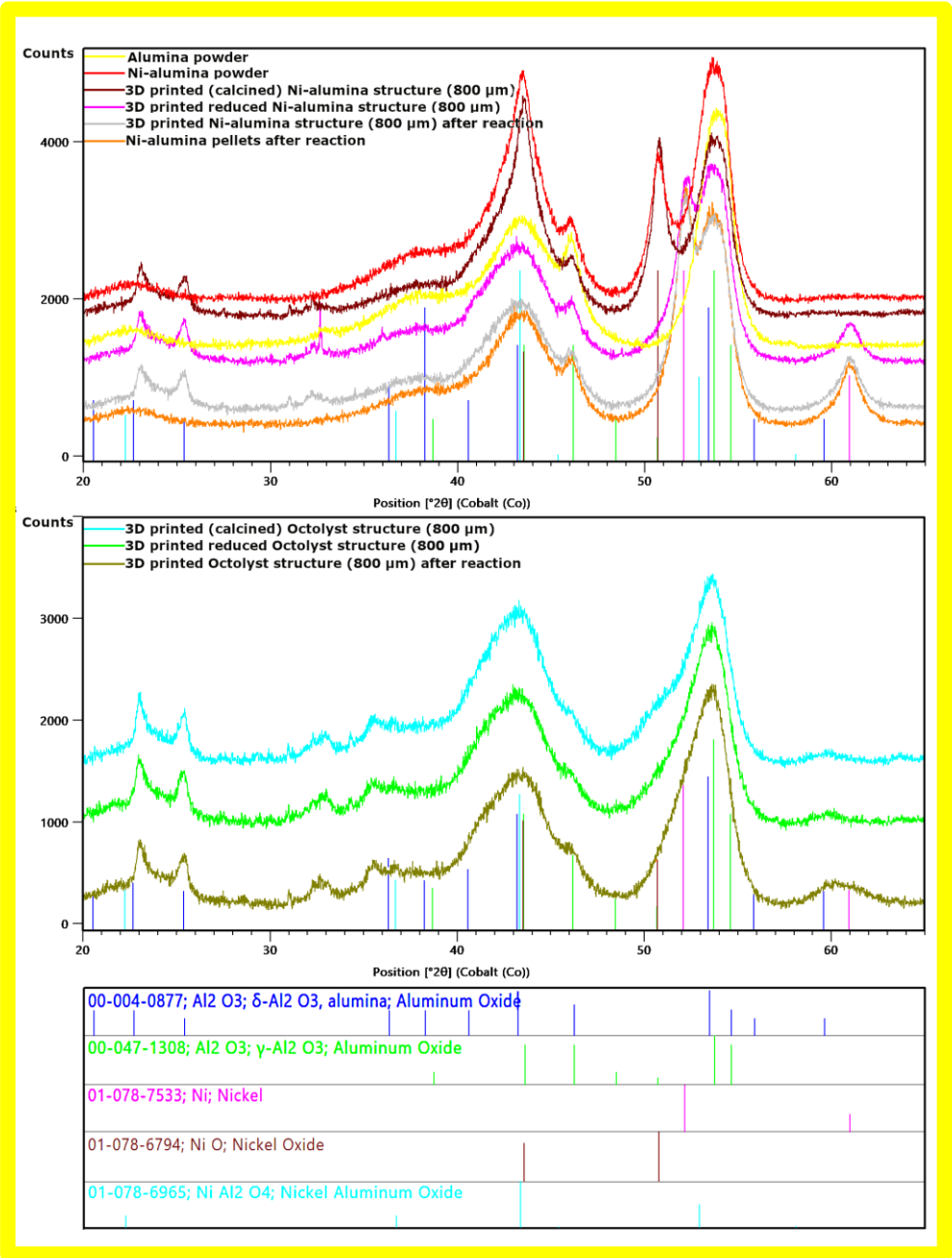

Figure 3. XRD diffractograms of 3D printed Ni-alumina (top) and Octolyst (bottom) samples after calcination, reduction and reaction showing the region between 20 and 70° 2θ in more detail. Indexing lines for the positively identified phases present in the patterns are given below.

3.2 Catalyst activity

The catalysts were evaluated based on their performance in the CO_2 methanation experiments and achieved CO_2 conversion, CH_4 yield and CH_4 selectivity (see Figure 4). In addition, previously reported values (Danaci et al, 2016, 2018)[54] for Ni coated 3D-SS and 3D-Cu were added to this comparison (wherein 3D-SS is a 3D printed stainless steel structure and 3D-Cu a 3D printed Cu structure).

The top plot in **Error! Reference source not found.** shows the CO_2 conversion per catalyst as a function of temperature (see in addition the thermal equilibrium conversion of the reaction which is plotted against the temperature). The 3D printed Octolyst exhibits the highest levels of conversion at all the temperatures, which is due to the thermodynamic equilibrium position favouring conversion. The results for both 3D printed catalysts show high activity at temperatures around 350°and a slight decrease in activity at rising temperatures between 350 and 450 °C. This trend is consistent with what has been reported elsewhere: the equilibrium favours methanation which is an exothermic reaction takingplace at lower temperatures. In contrast, Ni-alumina pellets and beads show an increase in conversion and yield with increasing reaction time. Pellet-shaped catalysts have comparable conversion rates to one another, at 400 and 450 °C. The impregnated 1.0 mm beads have the lowest CO_2 conversion and CH_4 yield in comparison to the samples manufactured by 3D printing (the stuctures and their crushed and pelletised equivalents). This shows that the shape of the catalyst plays a role in the reactions.

The effect of the morphology (macroporosity and geometry) of the catalyst on the reaction can clearly be seen in the selectivity data. It is shown that the selectivity towards CH_4 for all the catalyst decreases with an increasing temperature, except for 3D printed Ni alumina, which does not exhibit temperature dependence. According to Gao et al, (2012, 2015) increasing the reaction temperature above 450°C results in an increase in carbon monoxide as a by-product due to a reversed water gas shift reaction, alongside an increase in unreacted CO_2 and H_2, while the CH_4 product starts to decrease.

Regarding the effect of the geometry, the results for the 3D printed stainless steel and Cu coated structures (3D-SS and 3D-Cu, respectively) described by Danaci et al., 2016, 2018 are shown in Figure 4 for comparison showing opposing results: while the CH_4 yield for all the samples is at its highest at 350 °C, the coated structures show the maximum CH_4 yield at 450 °C. In particular their CH_4 selectivity (in Figure 4c), catches the eye as it displays the highest CH_4 selectivity (98 %) overall, slightly above that of the 3D printed Octolyst structure at both 350 °C and 400 °C. This can be explained by CO_2 conversion. When CO_2 conversion rates are lower (far removed from the equilibrium point), as is the case for the coated structures, the chances of forming by-products are limited due to high affinity for CH_4 formation (henceit is safe to assume that the reverse water-

gas shift reaction is negligable). Therefore, the main production of these coated structures will be CH_4, which explains their high CH_4 selectivity.

This substantial difference can be rationalised in terms of a number of factors including loading on the structure, coating thickness, different support structures, nickel distribution on th support, geometry and macroporosity. The radically different methods of the catalyst preparation and different measurement conditions (GHSV) prevent a straightforward comparison between these two structured forms.

In addition, the CH_4 productivity was calculated for each sample at set temperatures (350, 400 and 450°C). The results are given in **Error! Reference source not found.**. The productivity of the 3D printed Octolyst structures are higher than those of the other tested catalysts while the Ni impregnated beads show the lowest productivity. These results confirm the earlier conclusion that the highest catalytic activity (CH_4 yield, CH_4 selectivity and CO_2 conversion) can be obtained by 3D printing the commercial catalyst. A notably sharp drop in selectivity (corresponding to low but increasing conversion) observed for Ni-alumina pellets and Ni-alumina beads leads to a loss in productivity at temperatures from 350 ° C.

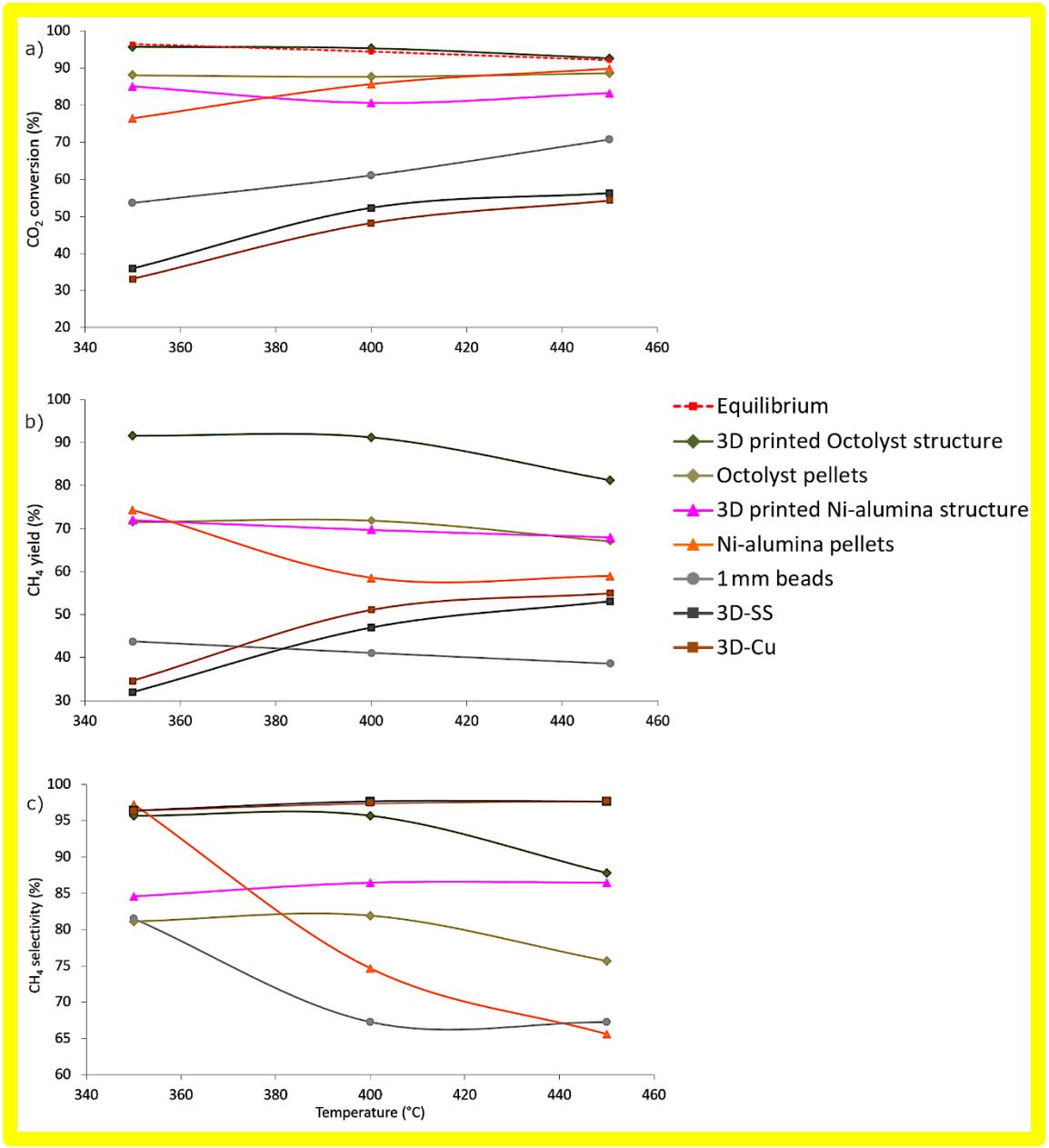
a)
CO_2 conversion (%)
b)
CH_4 yield (%)
c)
CH_4 selectivity (%)
Temperature (°C)
Equilibrium
3D printed Octolyst structure
Octolyst pellets
3D printed Ni-alumina structure
Ni-alumina pellets
1 mm beads
3D-SS
3D-Cu

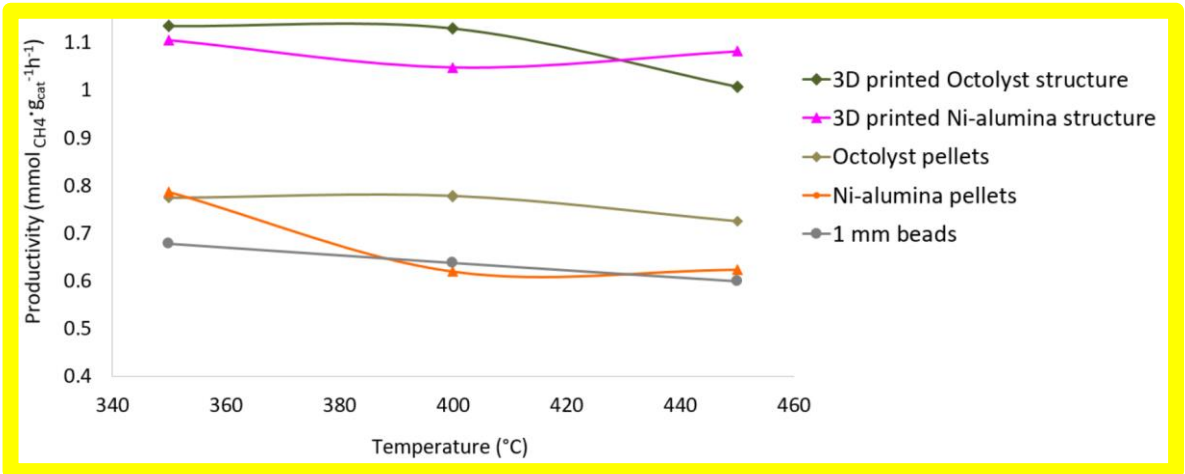
Productivity (mmol $_{CH4}$ $\cdot g_{cat}^{-1} h^{-1}$)
Temperature (°C)
3D printed Octolyst structure
3D printed Ni-alumina structure
Octolyst pellets
Ni-alumina pellets
1 mm beads

Figure 4. Comparison of a) CO_2 conversion, b) CH_4 yield and c) CH_4 selectivity d) catalyst productivity of all the examined samples at temperatures of 350, 400 and 450 °C, H_2:CO_2 ratio of 4:1 and at a GHSV of 3750 h^{-1} (total flow of 200 ml/min: 40 ml/min of H_2 and 10 ml/min of CO_2 in 150 ml/min of He) at 1 atm; the 3D printed Octolyst displayed all three points of conversion at the equilibrium maximum; corresponding thermodynamic equilibrium data points were calculated using the FactSage 7.2 software package[65]; 3D-SS and 3D-Cu were previously described by Danaci et al., 2016, 2018.

3.3 Catalyst stability

The 3D printed Octolyst catalyst was selected for further testing based on its superior activity. Possible catalyst deactivation during methanation has been monitored by mass spectrometry under methanation operating conditions at 350 °C and 300 °C, a GHSV of 2812.5 h^{-1} for 240 hours (see Figure 5). The measured data for the Octolyst structure were constant with small variations in CO_2 conversion and CH_4 yield between changes in flow rate and temperature (for further details on gas analysis see Figure S9 the Supplementary Information). However, both the MS and the previous GS measurements (shown in Figure 4) have confirmed that the highest conversions in this work were achieved for Octlyst at 350 °C which is in agreement with the data found in the literature on Ni-alumina based catalysts (as briefly mentioned in the introduction).

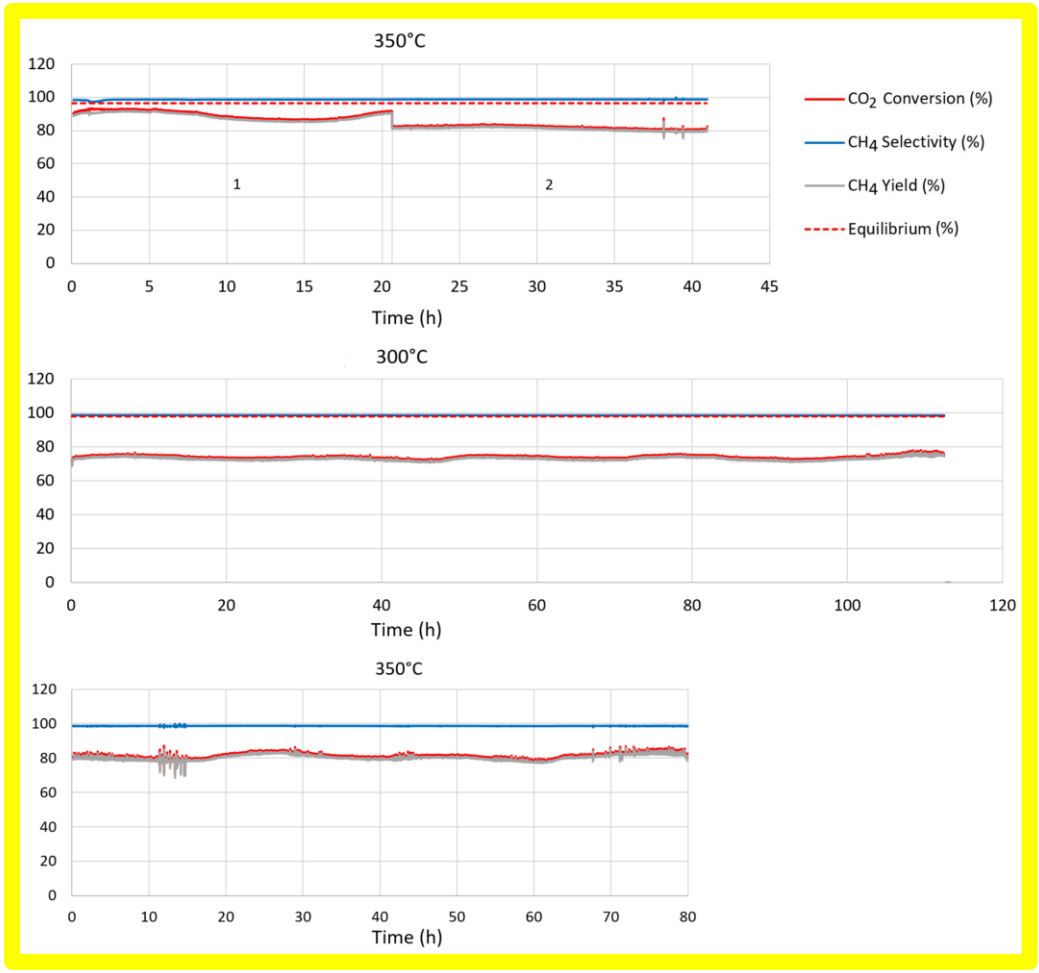

Figure 5. Comparison of consecutive MS measurements (CO_2 conversion, CH_4 yield, CH_4 selectivity data) during a total 240 h of methanation reaction over a 3D printed Octolyst structure at a GHSV of 2812.5 h^{-1}, 1 atm and at the following flow rates and temperatures: (top-1) 350 °C 40 ml/min of H_2, 10 ml/min of CO_2 in 100 ml/min of He (top-2, middle and bottom) 350 °C, 300 °C and 350 °C respectively at 80 ml/min of H_2, 20 ml/min of CO_2 in 50 ml/min of He.

3.4 XRD-CT studies under under *operando* conditions

In the XRD-CT data for the 3D printed Ni-alumina based catalyst, the majority of peaks present correspond to the γ-Al_2O_3 support (see Figure S10, Supplementary Material). The series of scans labelled "400 °C stacks" (shown in Figure 6) show reflections forming at ca. 1.77 and a shoulder at 2.04 Å at 400 °C under methanation operating conditions, corresponding to metallic face centred cubic (fcc) Ni. The data collected at 400 °C under methanation conditions also has a very broad peak in regions associated with fcc Ni. However, these are too broad to fit on a per pixel basis, indicating that they do not show extensive long-range order due to their being nanocrystalline. The 200 reflection (1.77 Å) increases in intensity/height between 1st stack and

$2^{nd}/3^{rd}$ stacks (at 400 °C under methanation operating conditions). The average crystallite size does not vary much, indicating that this is an increase in the amount of crystalline material and not due to sintering. The main 111 reflection at 2.04 Å cannot be fitted as it is a broad shoulder on the alumina peak at ca. 2.0 Å. Therefore the 200 reflection at 1.77 Å is used for fitting. Due to the metallic Ni shoulder, the Al_2O_3 peak at 2.00 Å is not used for fitting but the one at 1.40 Å is. For all measurements, no peaks are observed to disappear; no peaks attributable to NiO are present, so it may be that the initial form of the Ni is non-crystalline.

A Scherrer analysis from the profiling of the 200 reflection yields a support-average crystallite size of around 33 nm, with the majority of the distribution in the range of 30-35 nm. This is broadly consistent across the different data sets, however the final two stacks at 400 °C exhibit a small decrease in the average crystallite size to 29 nm. The metallic Ni has a crystallite size distribution of 15-20 nm.[66]

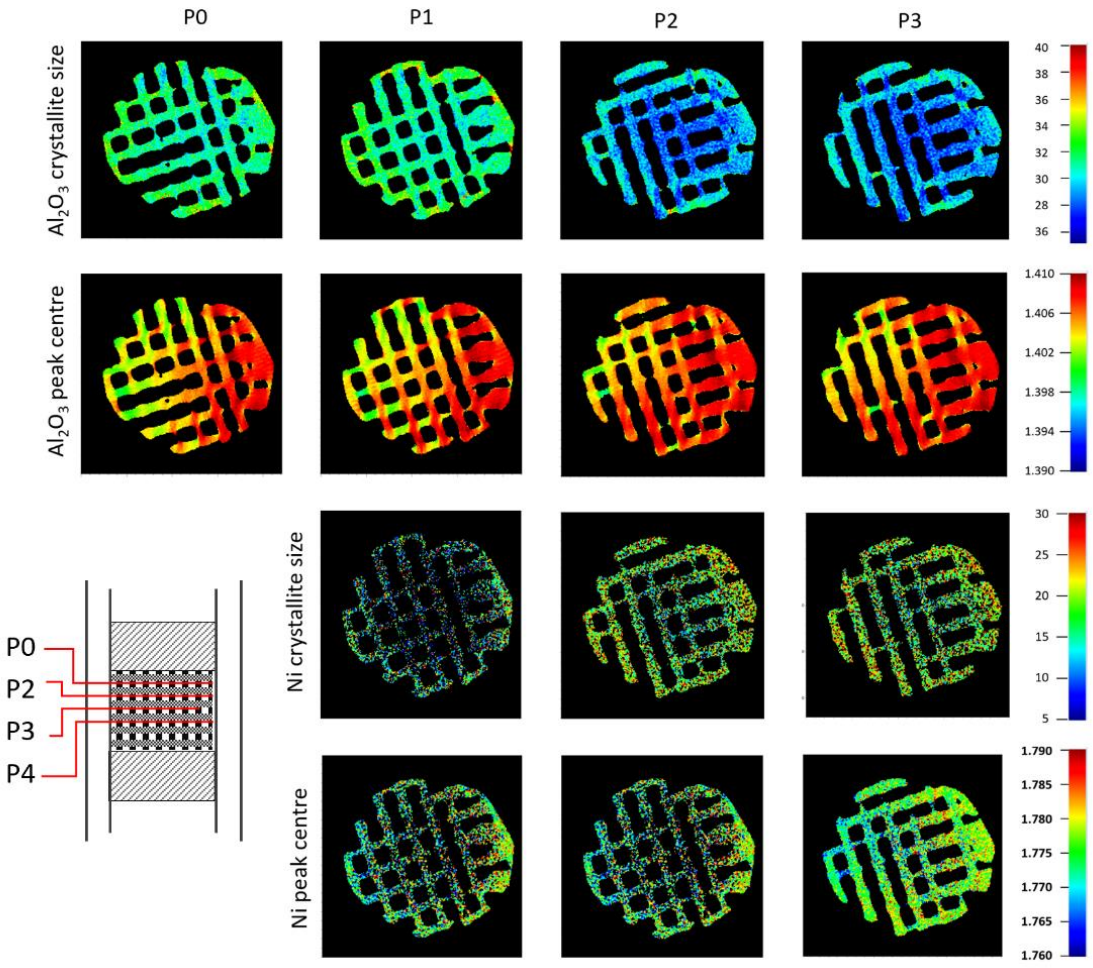

Figure 6. Reconstructed images '400 °C stacks' present four different positions across the 3D printed structure, PO,P1, P2, P3 (see columns corresponing to positions in a schematic in the bottom left corner) at 400°C under methanation operating conditions. Images within each panel

show: top row - Al_2O_3 average crystallite size, colour scale bar 25-40 nm; second row: Al_2O_3 peak centre position, colour scale bar 1.390-1.410 Å; third row: Ni fcc average crystallite size, colour scale bar 25-40 nm; bottom row: Ni fcc peak centre position, colour scale bar 1.760-1.790 Å.

For comparison, identical *operando* experiments were performed using the 3D printed in-house Ni-alumina and 3D printed commercial catalyst (Octolyst).

Some preliminary results from the *opearndo* experiment on the 3D printed in-house Ni-alumina catalyst are presented in Figures 8 (also see Figure S15 in the Supplementary Information). These maps are derived from the sum of the diffraction intensity of a peak of interest corresponding to Ni, NiO and Al_2O_3 after background subtraction. The maps shown in Figure 8 correspond to XRD-CT scans 1, 3, 5, 7 and 9 (top) and XRD-CT scans 2, 4, 6, 8 and 10 (bottom) - details of the experimental protocol are shown in Figure S14. The Al_2O_3 distribution is homogeneous; this is expected as it is the support of the catalyst. However, the crystalline Ni species seem to be less homogeneously distributed as there are regions of high concentration of this material (hotspots in Figure 8). The presence of NiO and Al_2O_3 was observed in the fresh catalyst; the presence of the spinel phase $NiAl_2O_4$ was confirmed by the lab XRD analysis. Upon reaching 450 °C, it can be seen that the NiO has reduced to metallic Ni.

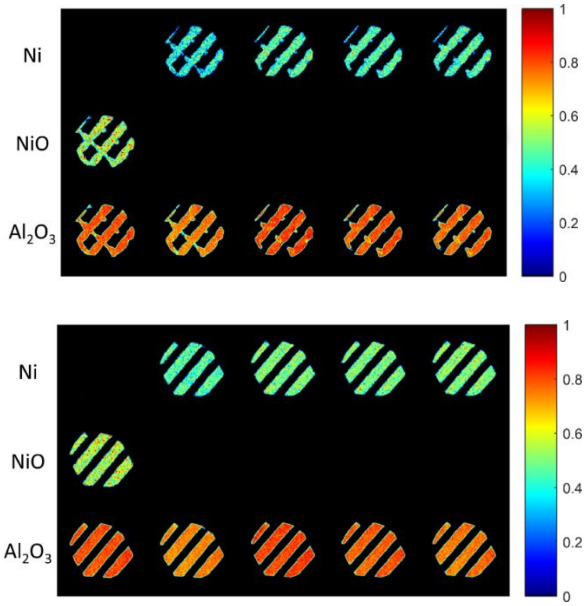

Figure 8. Phase distribution maps of Ni, NiO and Al_2O_3 for XRD-CT scans performed at two z position, at the top and bottom of the 3D printed Ni-alumina catalyst: top - XRD-CT scans 1, 3, 5, 7 and 9 and bottom - XRD-CT scans 2, 4, 6, 8 and 10 (see Figure S14 for details).

The XRD-CT datasets for the 3D printed Octolyst catalyst are presented in Figure 9 and Supplementary Figure S17 corresponding to the experimental protocol shown in Figure S16. It can be clearly seen that the main difference between the 3D printed Octloyst and the in-house

catalyst prepared is related to the Ni species. Specifically, the diffraction peaks corresponding to the NiO phase (and the Ni phase after the reduction/activation step) are seen to be broader for the Octolyst sample. This suggests that the Ni species are less crystalline with smaller crystallite size. The results presented in Figure 9 offer limited information as due to this broadening effect it was not possible to follow the same data processing strategy as in Figures 8. Therefore, these maps correspond to the summed intensity of certain diffraction peaks of interest without background subtraction. It is noteworthy, however, that the distribution of the Ni species appears to be more homogeneous in the Octolyst sample compared to the in-house sample. In order to extract more information from these datasets it is necessary to perform Rietveld analysis.

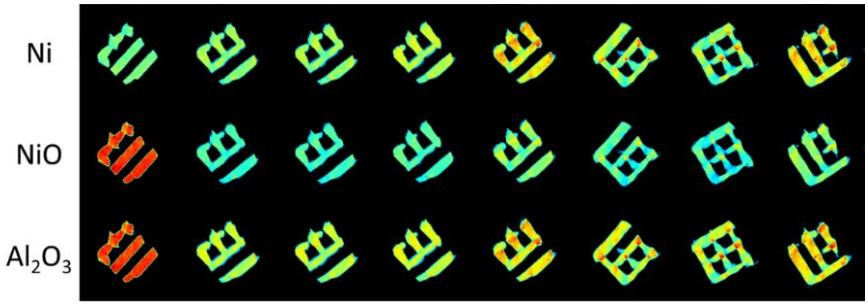

Figure 9. Phase distribution maps of Ni, NiO and Al_2O_3 for the 3D printed Octolyst catalyst (background has not been subtracted): XRD-CT scans 1-8 (see Figure S16 for details).

4. Conclusions

Nickel-alumina based catalysts have been investigated as model systems for the design (3D printing) of monolithic structures for CO_2 methanation reactors. The structure-activity relationships of the 3D printed catalysts were explored under typical conditions for CO_2 hydrogenation to methane using the *operando* X-Ray Diffraction Computed Tomography (XRD-CT). The printed structures showed the potential to achieve optimal functionality and design (regular straight channel patterns) compared to the conventional randomly packed beds such as powders and granules. With 3D printing technologies on the cusp of bringing revolutionary changes to chemical engineering and catalysis, this work provides further impetus to the ongoing development of a series of monolithic/multi-channel components for reactor systems and devices with a high degree of flexibility for a wide range of chemistry and energy applications.

The tomographic 'chemical imaging' approach used demonstrates the importance of operando studies. The research presented herein reveals the evolution and spatial distribution of the active Ni-based species (in terms of both their crystalline phase and crystallite sizes) during their activation while operating under methanation conditions. These results can, in turn, be fed back into the 3D design of the catalyst structures.

In addition to the findings confirming the distribution of the Ni species to be more homogeneous in the 3D printed commercial catalysts (compared to the 3D printed in-house catalyst), the 3D printed commercial catalysts (Octolyst, Evonik) exhibit superior performance to other catalyst forms studied in this work (such as 3D printed in-house prepared Ni-alumina, pellets and beads) with conversion reaching equilibrium. The 3D printed Octolyst catalyst has the best performance at 350°C and 400°C as the formation of methane is thermodynamically favoured. From 400°C a steep decrease in its CH_4 yield and selectivity is observed. It can be seen that 3D printed structures show highest activity, followed by their pellet shaped counterparts. The performance of Octolyst in the shape of pellets shows the same trend as its printed equivalent and confirms the advantage of 3D printing. The 3D printed in-house prepared Ni-alumina shows less catalytic activity at 350°C and 400°C but still comparable to the Octolyst pellets. The Ni impregnated alumina spheres show the lowest CO_2 conversion, CH_4 selectivity and yield. Crucially, when other reaction parameters were kept constant, the samples with different geometries displayed different temperature dependence as can be seen from the significant variation in selectivity with temperature. At the same time, they have similar trends in a gradual loss in productivity, indicative of CO_2 consumption. This can be attributed to the simultaneous occurrence of the reverse water gas shift reaction leading to the unreacted CO_2 and H_2 forming the undesired product, carbon monoxide.

Acknowledgements

The authors wish to acknowledge Sasol Performance Chemicals, Inorganics & Catalysts Division, Germany for kindly supplying commercial grade Puralox alumina and Evonik Resource Efficiency GmbH, Germany for kindly providing Octolyst® catalyst samples. The authors would like to thank the ESRF for the beamtime (proposals CH4782 and CH5329), and the staff of beamline ID15A for assistance with the catalytic testing and acquisition of the XRD-CT data presented in this paper. All the authors also gratefully acknowledge the financial support provided by their respective institutions.

[1] Novel Carbon capture and utilisation technologies, Group of Chief Scientific Advisors, Chief Scientific Advisors Scientific Opinion 4/2018, https://ec.europa.eu/research/sam/pdf/sam_ccu_report.pdf

[2] S. J. Bennett, D. J. Schroeder, S. T. McCoy, Towards a framework for discussing and assessing CO2 utilisation in a climate context, Energy Procedia, 2014, 63, 7976 – 7992.

[3] C. Breyer, E. Tsupari, V. Tikka, P. Vainikka, Power-to-gas as an emerging profitable business through creating an integrated value chain, Energy Procedia, 2015, 73, 182–189.

[4] C. Vogt, M. Monai, G. J. Kramer, B. M. Weckhuysen, The renaissance of the Sabatier reaction and its applications on Earth and in space, Nature Catalysis, 2019, 2, 188–197.

[5] W. Wei, G. Jinlong, Methanation of carbon dioxide: an overview, Front. Chem. Sci. Eng. 2011, 5, 2-10.

[6] ENEA Consulting. The potential of power-to-gas, Technology review http://www.enea-consulting.com/wp-content/uploads/2016/01/enea-consulting-the-potential-of-power-to-gas.pdf, 2016.

[7] S.A. Scholten, J.D. Allison, B.C. Dunn, Methanation reaction methods utilizing enhanced catalyst formulations and methods of preparing enhanced methanation catalysts, 2014, http://www.google.co.uk/patents/us8754137

[8] S. M. Jarvis, S. Samsatli, Technologies and infrastructures underpinning future CO2 value chains: A comprehensive review and comparative analysis, Renewable and Sustainable Energy Reviews, 2018, 85, 46–68.

[9] K.P. Brooks, J. Hu, H. Zhu, R.J. Kee, Methanation of carbon dioxide by hydrogen reduction using the Sabatier process in microchannel reactors, 2007, Chem Eng Sci, 62, 1161-1170

[10] S. Pérez, J. J. AragónlÑigo Peciña, E.J. Garcia-Suarez, Enhanced CO2 Methanation by New Microstructured Reactor Concept and Design, Topics in Catalysis, 2019, 1–6, https://doi.org/10.1007/s1124

[11] C. Janke, M.S. Duyar, M. Hoskins, R. Farrauto, Catalytic and adsorption studies for the hydrogenation of CO2 to methane, Appl. Catal. B Environ. 2014, 152–153, 184–191.

[12] M. Götz, J. Lefebvre, F. Mörs, A. McDaniel Koch, F. Graf, S. Bajohr, R. Reimert, T. Kolb, Renewable Power-to-Gas: A technological and economic review, Renewable Energy, 2016, 85, 2016, 1371-1390

[13] M. Lehner, Methanation process development utilizing ceramic honeycomb catalysts, in: 3rd Nuremb. Work. Methanation Second Gener. Fuels, 2016, 1–6.

[14] A. Vita, C. Italiano, . Pino, P. Frontera, M. Ferraro, V. Antonucci, Activity and stability of powder and monolith-coated Ni/GDC catalysts for CO2 methanation, Applied Catalysis B: Environmental, 2018, 226, 384-395.

[15] C. Fukuhara, K. Hayakawa, Y. Suzuki, W. Kawasaki, R. Watanabe. A novel nickel-based structured catalyst for CO 2 methanation: A honeycomb-type Ni/CeO2 catalyst to transform greenhouse gas into useful resources. Applied Catalysis A: General, 2017, 532, 12–18.

[16] M. Frey, D. Édouard, A.-C. Roger, Optimization of structured cellular foam-based catalysts for low-temperature carbon dioxide methanation in a platelet milli-reactor, Comptes Rendus Chim., 2015, 18, 283–292.

[17] E. Bianchi, T. Heidig, C. G. Visconti, G. Groppi, H. Freund, E. Tronconi, An appraisal of the heat transfer properties of metallic open-cell foams for strongly exo-/endo-thermic catalytic processes in tubular reactors, Chem. Eng. J. 2012, 198–199, 512–528.

[18] G.M. Gratson, M. Xu, J.A. Lewis, Direct writing of three-dimensional webs, Nature, 2004, 428, 386
[19] J.A. Lewis, G.M. Gratson, Direct writing in three dimensions, Materials Today 2004 7, 7–8, 32-39
[20] J.A. Lewis, Direct ink writing of 3D functional materials. Adv. Funct. Mater. 2006, 16, 2193–2204.
[21] R.L. Truby, J.A. Lewis, "Printing Soft Matter in Three Dimensions, Nature 2016, 540, 371-378.
[22] J.A. Lewis, B.Y. Ahn. Device Fabrication: Three-dimensional printed electronics, Nature 2015, 518, 42-43.

[23] A.S. Gladman, E.A. Matsumoto, R.G. Nuzzo, L. Mahadevan, J.A. Lewis. Biomimetic 4D Printing, Nature Materials 2016, 15, 413-419.

[24] C. Parra-Cabrera, C. Achille, S. Kuhn, R. Ameloot, 3D printing in chemical engineering and catalytic technology: Structured catalysts, mixers and reactors, Chemical Society Reviews, 2018,47, 209-230

[25] C. W. Hurt, M. Brandt, S. S. Priya, T. Bhatelia, J. Patel, PR. Selvakannan, S. Bhargava, Combining Additive Manufacturing and Catalysis: A Review, Catalysis Science & Technology, 2017, 7, 3421-3439.

[26] X. Zhou, C-J. Liu, Three-dimensional Printing for Catalytic Applications: Current Status and Perspectives, Advanced Functional Materials 2017, 27(30), 1701134.

[27] C.R. Tubío, J. Azuaje, L. Escalante, A. Coelho, F. Guitián, E. Sotelo, A. Gil, 3D printing of a heterogeneous copper-based catalyst. *J. Catal* 2**016**, *334*, 110–115.

[28] J. Azuaje, C.R. Tubío, L. Escalante, M. Gómez, F. Guitián, A. Coelho, O. Caamaño, A. Gil, E. Sotelo, An efficient and recyclable 3D printed α-Al2O3 catalyst for the multicomponent assembly of bioactive heterocycles. Appl Catal A*,* 2017, *530*, 203–210.

[29] A.S. Díaz-Marta, C.R. Tubío, C. Carbajales, C. Fernández, L. Escalante, E. Sotelo, F. Guitián, V.L. Barrio, A. Gil, A. Coelho, Three-Dimensional Printing in Catalysis: Combining 3D Heterogeneous Copper and Palladium Catalysts for Multicatalytic Multicomponent Reactions, ACS Catal. 2018, 8, 1, 392-404.

[30] X. Li, F. Rezaei, A.A. Rownaghi, Methanol-to-olefin conversion on 3D-printed ZSM-5 monolith catalysts: Effects of metal doping, mesoporosity and acid strength, Microporous and Mesoporous Materials, 2019, 276, 1-12.

[31] V. Middelkoop, T. Slater, M. Florea, F. Neațu, S. Danaci, V. Onyenkeadi, K. Boonen, B. Saha, I-A. Baragau, S. Kellici, Next frontiers in cleaner synthesis: 3D printed graphene-supported CeZrLa mixed-oxide nanocatalyst for CO2 utilisation and direct propylene carbonate production, Journal of Cleaner Production, 2019, 214, 606-614

[32] B. Miao, S. S. Khine Ma, X. Wang, H. Su, S. Hwa Chan, Catalysis mechanisms of CO2 and CO methanation, Catal. Sci. Technol., 2016, 6, 4048-4058

[33] W. Wang, S. Wang, X. Ma, J. Gong, Recent Advances in Catalytic Hydrogenation of Carbon Dioxide, Chemical Society Reviews 2011, 40(7), 3703-3727.

[34] K. Stangeland, D. Kalai, Z.Yu, CO2 Methanation: The Effect of Catalysts and Reaction Conditions, Energy Procedia, 2017, 105, 2022-2027.

[35] S. Rönsch, J. Schneider, S. Matthischke, M. Schlüter, M. Götz, J. Lefebvre, P. Prabhakaran, S. Bajohr, Review on methanation – From fundamentals to current projects, Fuel 2016, 166, 276–296

[36] P. Frontera, A. Macario, M. Ferraro, PL. Antonucci, Supported Catalysts for CO2 Methanation: A Review, Catalysts 2017, 7, 59

[37] C. Mebrahtu, F. Krebs, S. Abate, S. Perathoner, G. Centi, R. Palkovits, CO2 Methanation: Principles and Challenges. Horizons in Sustainable Industrial Chemistry and Catalysis, 2019, 85–103.

[38] J. Gao, Y. Wang, Y. Ping, D. Hu, G. Xu, F. Gu, F. Su, A thermodynamic analysis of methanation reactions of carbon oxides for the production of synthetic natural gas, RSC Advances, 2012, 2, 2358–2368.

[39] J. Gao, Q. Liu, F. Gu, B. Liu, Z. Zhong, F. Su, Recent advances in methanation catalysts for the production of synthetic natural gas. RSC Advances, 2015, 5(29), 22759–22776.

[40] J. Ashok, M.L. Ang, S. Kawi, Enhanced activity of CO_2 methanation over Ni/CeO_2-ZrO_2 catalysts: Influence of preparation methods, Catalysis Today, 2017, 281, 304-311.

[41] Y. Yu, Y. Meng Chan, Z. Bian, F. Song, J. Wang, Q. Zhong, S. Kawi, Enhanced performance and selectivity of CO2 methanation over g-C3N4 assisted synthesis of $NiCeO_2$ catalyst: Kinetics and DRIFTS studies, International Journal of Hydrogen Energy, 2018, 43, 15191-15204.

[42] Z. Bian, Y.M. Chan, Y. Yu, & S. Kawi, Morphology dependence of catalytic properties of Ni/CeO2 for CO2 methanation: A kinetic and mechanism study. Catalysis Today. (2018). DOI: 10.1016/j.cattod.2018.04.067

[43] J. Lin, C. Ma, Y. Xu, G. Ma, Jie Wang, H. Wang, C. Dong, C. Zhang, M. Ding, Enhanced low-temperature performance of CO_2 methanation over mesoporous Ni/Al2O3-ZrO2 catalysts, Applied Catalysis B: Environmental, 2019, 243, 262-272.

[44] J. Guilera, J. del Valle, A. Alarcón, J. A. Díaz, T. Andreu, Metal-oxide promoted Ni/Al2O3 as CO2 methanation micro-size catalysts, Journal of CO_2 Utilization, 2019, 30, 11-17.

[45] C.H. Bartholomew C.K. Vance, Effects of support on the kinetics of carbon hydrogenation on nickel Journal of Catalysis, 1985, 91(1), 78-84.

[46] C. V. Miguel, A. Mendes, L. M. Madeira, Intrinsic kinetics of CO_2 methanation over an industrial nickel-based catalyst, Journal of CO_2 Utilization, Volume 25, May 2018, 128-136

[47] R. A. Hubble, J. Y. Lim, J. S. Dennis, Kinetic studies of CO2 methanation over a Ni/γ-Al2O3 catalyst, Faraday Discuss., 2016, 192, 529-544.

[48] T. A. Le, Tae Wook Kim, Sae Ha Lee, and Eun Duck Park, CO and CO_2 methanation over Ni catalysts supported on alumina with different crystalline phases, Korean Journal of Chemical Engineering, 2017, DOI: 10.1007/s11814-017-0257-0

[49] X. Guo, A. Traitangwong, M. Hu, C. Zuo, V. Meeyoo, Z. Peng, C. Li, Carbon dioxide methanation over Nickel-based catalysts supported on various mesoporous material, Energy Fuels, 2018, 323, 3681-3689

[50] D. Beierlein, D. Häussermann, M. Pfeifer, T. Schwarz, K. Stöwe, Y. Traa, E. Klemm, Is the CO2 methanation on highly loaded Ni-Al2O3 catalysts really structure-sensitive? Applied Catalysis B: Environmental, 2019, 247, 200-219.

[51] F.W. Chang, M.S. Kuo, M.T. Tsay, M.C. Hsieh, Hydrogenation of CO2 over nickel catalysts on rice husk ash-alumina prepared by incipient wetness impregnation, Appl. Catal. A Gen. 2003, 247, 309–320

[52] S. Rahmani, M. Rezaei, F. Meshkani, Preparation of highly active nickel catalysts supported on mesoporous nanocrystalline γ-Al2O3 for CO_2 methanation, Journal of Industrial and Engineering Chemistry, 2014, 20, 4, 1346-1352

[53] Z. Zhang, Y. Tian, L. Zhang, S. Hu, X. Hu, Impacts of nickel loading on properties, catalytic behaviors of Ni/γ–Al2O3 catalysts and the reaction intermediates formed in methanation of CO_2, International Journal of Hydrogen Energy, 2019, 44(18), 9291-9306

[54] (a) S. Danaci, L. Protasova, J. Lefevere, L. Bedel, R. G. Marty, Efficient CO_2 methanation over Ni/Al_2O_3 coated structured catalysts, Catal. Today 2016, 273, 234-243; (b) S. Danaci, L. Protasova, F. Snijkers, W. Bouwen, A. Bengaouer, P. Marty, Innovative 3D-manufacture of structured copper supports post-coated with catalytic material for CO_2 methanation, Chemical Engineering and Processing - Process Intensification, 2018, 127, 168-177

[55] S. Danaci, L. Protasova, V. Middelkoop, N. Ray, M. Jouve, A. Bengaouer, P. Marty, React. Chem. Eng., (2019), DOI: 10.1039/c9re00092e

[56] M.G. O'Brien, S.D.M. Jacques, M. Di Michiel, P. Barnes, B.M. Weckhuysen and A. M. Beale, Active phase evolution in single Ni/Al_2O_3 methanation catalyst bodies studied in real time using combined μ-XRD-CT and μ-absorption-CT, Chem. Sci., 2012, 3, 509–523

[57] A. M. Beale, S. D. Jacques, B. M. Weckhuysen, Chemical imaging of catalytic solids with synchrotron radiation. Chemical Society reviews, 2010, 39, 4656-4672.

[58] A. M. Beale, S. D. M. Jacques, E. L. Gibson, M. Di Michiel, Progress towards five dimensional diffraction imaging of functional materials under process conditions. Coord. Chem. Rev. 2014, 277–278, 208–223.

[59] A. Vamvakeros, S D. M. Jacques, V. Middelkoop, M. Di Michiel, C. K. Egan, I. Z. Ismagilov, G. B. M. Vaughan, F. Gallucci, M. van Sint Annaland, P. R. Shearing, R. J. Cernik, A. M. Beale, Real time chemical imaging of a working catalytic membrane reactor during oxidative coupling of methane. Chem Commun 2015, 51, 12752-12755.

[60] A. Vamvakeros, S. D. M. Jacques, M. Di Michiel, D. Matras, V. Middelkoop, I. Z. Ismagilov, E. V. Matus, V. V. Kuznetsov, J. Drnec, P. Senecal, A. M. Beale, 5D operando tomographic diffraction imaging of a catalyst bed, Nature Comm, 2018, 9, 4751.

[61] Shaped carriers, Sasol, http://www.sasolgermany.de/fileadmin/doc/alumina/Neu_2017/Sasol_Shaped_Carriers_Flyer_07_08_17_23-00_Webversion_Einzelseiten.pdf.; http://www.sasolgermany.de/fileadmin/doc/alumina/121015_Spheres_Extrudates_Shapes.pdf; High-Purity Calcined Aluminas," http://www.sasolnorthamerica.com/Images/Interior/products/sasol-inorganics_puralox_catalox%20(2).pdf

[62] J. Lefevere, L. Protasova, S. Mullens, V. Meynen, 3D-printing of hierarchical porous ZSM-5: The importance of the binder system, Materials & Design, 2017, 134, 331-341.

[63] V. Middelkoop, K. Coenen, J. Schalck, M. Van Sint Annaland, F. Gallucci, 3D printed versus spherical adsorbents for gas sweetening, Chemical Engineering Journal, 2019, 357, 309-319.

[64] A. Vamvakeros, S. D. M. Jacques, M. Di Michiel, P. Senecal, V. Middelkoop, R. J. Cernik and A. M. Beale, Interlaced X-ray diffraction computed tomography, J. Appl. Cryst., 2016, 49, 485-496.

[65] C.W. Bale, E. Bélisle, P. Chartrand, S.A. Decterov, G. Eriksson, A.E. Gheribi, K. Hack, I.H. Jung, Y.B. Kang, J. Melançon, A.D. Pelton, S. Petersen, C. Robelin, J. Sangster, P. Spencer, M.A. Van Ende, FactSage thermochemical software and databases, 2010–2016, CALPHAD: Computer Coupling of Phase Diagrams and Thermochemistry, 2016, 54, 35–53

[66] G. Garbarino, P. Riani, L. Magistri, G. Busca, A study of the methanation of carbon dioxide on Ni/Al2O3 catalysts at atmospheric pressure, International Journal of Hydrogen Energy, 2014, 39 (22), 11557-11565.